Assessment of satellite-derived shorelines automatically extracted from Sentinel-2 imagery using SAET

J.E. Pardo-Pascual [a], J. Almonacid-Caballer [a], C. Cabezas-Rabadán [a,b,*], A. Fernández-Sarría [a], C. Armaroli [c], P. Ciavola [d,e], J. Montes [d,f], P.E. Souto-Ceccon [d], J. Palomar-Vázquez [a]

[a] Geo-Environmental Cartography and Remote Sensing Group (CGAT-UPV), Department of Cartographic Engineering, Geodesy and Photogrammetry, Universitat Politècnica de València, Camí de Vera S/n, Valencia, Spain
[b] Univ. Bordeaux, CNRS, Bordeaux INP, EPOC, UMR 5805, F-33600, Pessac, France
[c] Department of Biological, Geological and Environmental Sciences, University of Bologna Alma Mater Studiorum, Bologna, Italy
[d] Department of Physics and Earth Sciences, University of Ferrara, Ferrara, Italy
[e] Consorzio Futuro in Ricerca, Ferrara, Italy
[f] Department of Earth Sciences, International Campus of Excellence of the Sea (CEI·MAR), University of Cádiz, Cádiz, Spain

ABSTRACT

The definition of the shoreline position from satellite imagery is of great interest among coastal monitoring techniques. Understanding the reality mapped by the resulting shorelines and defining their accuracy is of paramount importance. The assessment described in this paper constitutes a validation of the shorelines obtained by using the novel tool SAET (Shoreline Analysis and Extraction Tool) for automatic shoreline extraction. The resulting shorelines applying the different parameters available in SAET are assessed in 9 test sites with diverse morphology and oceanographic conditions along the Atlantic European and Western Mediterranean coasts. The reference data is obtained along large coastal segments (covering up to about 240 km) from nearly coincident very high-resolution satellite images.

Different image processing levels and extraction methods have been tested, showing their key role in the accuracy of shoreline position. When defining the approximate shoreline position the Automated Water Extraction Index for images without shadows (AWEInsh) with a 0 threshold generally constitutes the best segmentation method. In turn, the employment of the mathematical morphological operations of dilation or erosion considerably improves the results in certain coastal typologies. On the contrary, the employment of atmospherically-corrected images has a smaller influence on the accuracy of the SDSs.

Results support the idea that the magnitude of the errors is strongly related to the specific coastal conditions- In general, the lowest errors appear in low-energetic microtidal sites, contrary to the energetic and mesotidal coasts with gentle slopes.

The shoreline errors range between 3.7 m and 13.5 m RMSE (root-mean-square error) among the different coastal types when selecting the most appropriate extraction parameters. The shoreline position identified with SAET shows a similar or better accuracy to that obtained by other tools.

1. Introduction

Coastal territories and sandy beaches undergo great morphological variations, in which the shoreline, defined here as the land-water interface, experiences important changes at different spatial and temporal scales. Efficient management of coastal areas requires a good characterisation and understanding of such changes, for which the availability of accurate and up-to-date data is essential. However, the data collection by employing traditional methods such as topographic surveys (e.g., Morton et al., 1993; Pardo-Pascual et al., 2005) severely limits the spatial or temporal data coverage, while the use of techniques

such as UAVs and terrestrial laser scanning (e.g., Casella et al., 2020; Duo et al., 2021; Guisado-Pintado et al., 2019; Talavera et al., 2018) requires field surveys that generate significant costs. In this context, various sources of Earth observation data can provide information with great potential to characterise coastal morphological changes over large areas and with high temporal resolution. This is the case of the optical imagery of the Sentinel-2A and 2B satellites (supplied by the European Commission through the European Space Agency, ESA), as well as the Landsat series (supplied by NASA). All of them acquire images covering large extensions (i.e., tens of kilometres) with short revisit times (5 days for Sentinel-2 when combined at the equator, with shorter revisit

intervals at higher latitudes (Bergsma and Almar, 2020).

Large SDS packages may allow to characterise the morphological response to storm events and anthropogenic actions (Cabezas-Rabadán et al., 2019a;b; Pardo-Pascual et al., 2014) and their consequences on the beach functions (Cabezas-Rabadán et al., 2019c). The Shoreline Analysis and Extraction Tool (SAET, Palomar-Vázquez et al., 2023) has been developed to carry out the automatic detection of the shoreline positions associated with the storm events using the images from the Sentinel satellites of the EU Copernicus program and the Copernicus Contributing Missions. Based on the tool SHOREX (Cabezas-Rabadán et al., 2021; Sánchez-García et al., 2020) SAET has been developed within the framework of the ECFAS project (A proof of concept for the implementation of a European Copernicus coastal flood awareness system, GA n° 101,004,211, www.ecfas.eu) focusing on achieving high autonomy and efficiency, capacity to be applied on large coastal segments, and robustness when working on different coastal types. The ECFAS Project aimed at developing tools and products for the evolution of the Copernicus Emergency Management Service (CEMS). ECFAS included the quantification of the shoreline displacement at pan-EU level on low-lying coasts in the aftermath of storm events using SDSs extracted from Landsat and Sentinel images. ECFAS has demonstrated that the shoreline analysis could represent an added-value product in the CEMS mapping component (https://emergency.copernicus.eu/mapping/) for emergency response and recovery actions as well as within the Copernicus Land Monitoring Service.

Different algorithms and methods have been developed to define the water boundary from Sentinel-2 and Landsat imagery while overcoming the limitations of the pixel size of the images (e.g., Bishop-Taylor et al., 2019; Hagenaars et al., 2018; Liu et al., 2017; Pardo-Pascual et al., 2012; Song et al., 2019; Viaña-Borja and Ortega-Sánchez, 2019; Vos et al., 2019a; see review and benchmark comparison in Vos et al., 2023). Most of the available approaches, especially those based on the analysis of the maximum gradient (Vitousek et al., 2023a), start by defining the shoreline at the pixel level so that, afterwards, a refining process leads to a finer sub-pixel shoreline definition.

The identification of the shoreline at the pixel level is still a matter of discussion in the literature (Pekel et al., 2016). To facilitate the definition of the coast, not only the original bands have been considered but also alternatives such as the Hue-Saturation-Value (HSV) transformation or the combinations of bands (indices). Among the latter ones, it is worth highlighting some specific indices suitable for thresholding water bodies: the Normalized Difference Water Index, NDWI (Gao, 1996), its modified version, MNDWI (Xu, 2006), and the Automated Water Extraction Index, AWEI (Feyisa et al., 2014). The latter presents two versions: one considering the effect of shadows (AWEIsh) and another without considering them (AWEInsh). There are several ways to define the shoreline position by using bands and indices among which classification (e.g., Pekel et al., 2016; Vos et al., 2019a) and thresholding (e.g., Bishop-Taylor et al., 2019, Song et al., 2019; Viaña-Borja and Ortega-Sánchez, 2019) processes are the most common ones. Otsu's thresholding method (Otsu, 1979) is one of the favourite processes to binarize a given index. It achieves a good class separation by calculating the histogram of a given image and taking two (or more) zones so that the variance inside each class is minimised. In turn, k-means (Mac-Queen, 1967) appears as a general clustering method but its application on images is equivalent to a segmentation method. The k-means method is used for grouping data into k clusters by minimising the distances between data points and their respective cluster centroids. Otsu and k-means follow the same logic, minimising the internal variance of each class, although k-means is faster (Liu and Yu, 2009). Taking all of this into account, SAET allows the user to choose among three different methods for defining the approximate shoreline at pixel level: single threshold value, Otsu and k-means. Despite this enhanced versatility, once the image is binarized in water and land, the shoreline can be identified as the first line of land pixels in contact with water or the first line of water pixels in contact with the land. At a sub-pixel precision, the

influence of this morphological consideration as well as the employment of different morphological filters (Haralick et al., 1987) still remains to be evaluated.

The positioning and accuracy of the resulting shoreline can be affected by several factors not linked to the subpixel edge detection itself. This is the case of mismatching between images due to georeferencing issues (Almonacid-Caballer et al., 2017), and the atmospheric treatment of the images. Both NASA and ESA offer their Landsat and Sentinel-2 images with two processing levels: Top of Atmosphere (TOA or 1C) and Bottom of Atmosphere (BOA or 2 A) modes. The latter represents an attempt to remove the effect of the atmosphere on the reflectance values (ESA, 2015; Gascon et al., 2017). While the effects of the georeferencing have been proven to be limited, the atmospheric corrections on the shoreline extraction still need further testing.

As different beach morphologies and oceanographic characteristics may influence the accuracy of the resulting shorelines a required step for taking advantage of them is the evaluation of their accuracy. Their assessment implies comparing the position of the obtained shorelines against coincident reference lines. Techniques such as differential GNSS (DGNSS), video-monitoring, and high-resolution imagery or information derived from 3D data may be applied to define the reference shorelines. Nevertheless, all of them are at a certain point affected by a time lag with the satellite image acquisition and by the subjective interpretation of the morphological reality when defining the reference data. For instance, the DGNSS may enable the instantaneous delineation of the water/land boundary or the wet/dry shore limit, being less robust and accurate when the magnitude of the waves, the swash processes, and the time lag between the SDS and the reference line increase. Video-monitoring systems may acquire instantaneous images but only along short beach segments. Likewise, the photointerpretation may be affected by the subjectivity of the shoreline digitalisation, while the exact temporal coincidence with the satellite cannot be guaranteed. 3D information has been widely used, mostly through DEMs and cross-shore profiles taken by DGNSS; other sources like LiDAR or photogrammetry from UAVs are less used because of the more difficult repeatability. Given the 3D information, the main procedure is to extract the contour line at a specific height, normally given by the tidal level and other effects like the wave run-up. This procedure is also affected by some limitations: on the one hand, the fact that the evolution of the beach might have not been recorded by the DGNSS campaigns depending on their revisit frequency or, on the other hand, run-up estimation is based on empirical parameterisations which could show large biases in some conditions (Stockdon et al., 2006). The aforementioned limitations cannot be avoided, and every accuracy evaluation must deal with them.

The aim of the present work is to evaluate the automatically extracted SDSs using the new software SAET. The results are focused on (a) the effect of the input images TOA and BOA and (b) the influence of the initial pixel-level shoreline on the final shoreline. The latter effect is influenced by both the band or index, the thresholding method, and the morphological filter used for deriving the pixel-level shoreline from the land/water mask. The tests are run over different sites that enable the analysis of the robustness of the resulting shorelines over different environments.

The work is organized in different sections. Firstly, the sites in which the assessment was carried out are presented together with the very high resolution (VHR) images employed as reference data. The methodology describes the shoreline definition and how the accuracy was assessed. The results section presents the errors for all the evaluation cases. The discussion and conclusion analyse the errors of the resulting shorelines in the context of different coastal types when using different combinations of image processing level, morphological filters and segmentation methods.

2. Test sites and material

The assessment was based on the comparison of SDSs extracted from

Sentinel-2 (hereafter S2) imagery using SAET with reference shorelines, extracted from nearly coincident Very High Resolution (VHR) images and considered in this study as ground-truth. VHR images were made available for this study through the Data Warehouse Mechanisms of ESA in the framework of the ECFAS project. The assessment was carried out at nine sites in order to test the performance of SAET under different characteristics.

2.1. Test sites

The sites for testing the SDSs were selected based on the availability of nearly coincident VHR images (Table 2, to be used as ground-truth) and on different parameters such as the tidal range, wave climate, exposure, and morphology (Fig. 1, Table 1). On the North Sea, the sites of Texel (site 1 in Fig. 1), Leiden (2 in Fig. 1) and The Hague (3, Fig. 1) are located on the Dutch coast, with an NNE-SSO orientation. Texel is located in the southernmost barrier island of the Wadden Sea, where approximately 30 km of the coast is a sandy beach exposed to the North Sea with sediment between fine and medium sand with D50 ranging from 0.21 to 0.39 mm (Galiforni-Silva et al., 2018), although the average value on the beach is around 0.25 mm (Elias and Van der Spek, 2017; Strypsteen et al., 2021). The area is a semidiurnal tidal environment with an average tidal range of 1.4 m, with a spring tidal range of 2 m (Galiforni-Silva et al., 2022). The waves usually come from N and SW, with a mean significant wave height of 1.48 and 1.44 m, typically no higher than 3 m, although during severe storm conditions it may exceed 4.5 m (Elias and Van der Spek, 2017). Leiden and The Hague extend continuously for more than 60 km, from the Amsterdam harbour access canal to the Rotterdam harbour access canal. The area is characterised by a uniform beach profile, with the presence of nearshore bars and a dune system (Luijendijk et al., 2017). The tide is semidiurnal asymmetric, which generates asymmetrical tidal currents, with a spring tidal range of 1.98 m (Luijendijk et al., 2017). The mean significant wave height is 1.7 m during the winter, although it can reach values higher than 4.5 m, normally from W and NW (Luijendijk et al., 2017). The D50 is 0.24 mm (Wijsman and Verduin, 2011).

From the Bay of Biscay, on the South-West Atlantic coast of France, two sites are considered. The area presents a mesotidal regime (spring tidal range of 4.5 m), and the wave climate is moderate to highly energetic (Morichon et al., 2018). The first one, Tarnos (4, Fig. 1), covers 2.9 km of open sandy beaches with D50 = 0.3 mm (Morichon et al., 2018) following an NNE-SSO orientation northern to the mouth of the Adour River. The second one, Saint-Jean-de-Luz (5 in Fig. 1, hereafter SJDL) covers 13.6 km of the coast between la Grande Plage Beach in Saint-Jean-de-Luz, and Cote des Basques Beach in Biarritz. The southern part includes several pocket beaches facing the NNO, while the northern part includes open beaches with an NNE-SSO orientation.

In Western Portugal, the site of Mira (6, Fig. 1) includes 23.7 km of a wave-dominated meso-tidal beach segment facing the North Atlantic Ocean with NNE-SSW orientation. The site belongs to a sandy barrier with a dune system and is eastward limited by the Aveiro lagoon. The beach presents medium-sized sand (D50 about 0.4 mm) uniform along space (Fontán-Bouzas et al., 2022) and is dominated by the North Atlantic swell, (mean annual Hs = 2 m, Tp = 7–15 s), exceeding 8 m during storms (Silva et al., 2009). The tidal regime is semidiurnal, with a tidal range between 2.8 m and 1.2 m for the spring and neap tides (Fontán-Bouzas et al., 2022).

Three sites from the Western Mediterranean were included in the assessment. The northern one, the Ebro (7, Fig. 1) covers 44.5 km of beaches of the Ebro Delta, while the sites of Castellón (8, Fig. 1) and Valencia (9, Fig. 1) include respectively 39.5 and 25.5 km of beaches along the Gulf of Valencia. The three Mediterranean sites are sedimentary wave-dominated micro-tidal environments with a tidal range of approximately 0.25 m (Grases et al., 2020; Pardo-Pascual and Sanjaume, 2019) although the combination of the astronomical and meteorological tides can lead to variations up to 1 m (Sierra et al., 2001). Mean wave conditions are quite similar in the three sites. For the Ebro site, the mean significant wave height (Hs) is 0.75 m, and the mean wave period (Tm) is 3.9 s in Ebro (Jiménez et al., 1997a); in Valencia the mean Hs is 0.7 and the mean wave period is 4 s (Cabezas-Rabadán et al., 2021). The energetic waves from the east and northeast are the predominant cause of morphological changes, with the storm waves exceeding 2 m (Sánchez-Arcilla et al., 2010; Pardo-Pascual and Sanjaume, 2019). The zone is characterised by a north-to-south drift, with the exception of the north side of the delta (Aranda-García et al., 2022). Regarding the geomorphological characteristics, the Ebro slope ranges between 0.03 and 0.23 at the swash zone (Jiménez et al., 1997b; Guillen and Palanques, 1997). Although fine sediments dominate most of the beach, grain sizes of 0.25–0.5 mm are the most common at the coastline (Guillen and Palanques, 1997). Castellón is mainly covered by coarser sands ranging between 0.4 and 3.65 mm (Pardo-Pascual and Sanjaume, 2019). The beach in Valencia is located at the southern side of its port and, while the median grain size is 0.5 mm, it decreases up to 0.25 mm when going southwards (Pardo-Pascual and Sanjaume, 2019).

2.2. Reference data: VHR images

In order to assess the spatial accuracy of the SDSs, nine VHR images were identified that coincide with the S2 imagery with a maximum time lag of the order of minutes between each other (Table 3). The VHR images allow the manual identification of a reference shoreline position to perform the assessment of SDSs accuracy on 9 different dates/locations. For this purpose, the images of the satellites Spot-6 (4 m/pixel) and Spot-7 (1.5 m/pixel), Pléiades 1 A y 1 B (0.5 m/pixel panchromatic product, 2 m/pixel multispectral product) and WorldView-2 (0.5 m/pixel) were employed.

Table 1
Characteristics of the test sites.

Site	Name	Coast	Location (Lat,lon)	Length of the analysed coastal tract (km)
1	Texel	North Sea, The Netherlands	53.112, 4.763	27.8
2	Leiden		52.348, 4.505	30.7
3	The Hague		52.118, 4.263	32.2
4	Tarnos	Bay of Biscay, SW France	43.543, −1.513	2.9
5	Saint-Jean-de-Luz		43.431, −1.603	13.6
6	Mira	W Portugal	40.456, −8.802	23.7
7	Ebro	W Mediterranean, E Spain	40.707, 0.873	44.5
8	Castellón		39.802, −0.128	39.5
9	Valencia		39.296, −0.286	24.5

Table 2

Summary of oceanographic conditions at the different test sites for the day and time of the S2 satellite images acquisition. Significant wave height, average and peak period, and tidal information. For the Mediterranean coasts, the data have been obtained from Puertos del Estado (https://www.puertos.es/), while for the Atlantic coasts, the data have been provided by Mercator Ocean International in the framework of the ECFAS project.

Site	Date (dd/mm/yy)	Time (UTC)	Hm0 (m)	Tp (s)	Sea surface height (m)	Tidal behavior	Tidal state	Tidal range (m)
1	30/06/2018	10:54	0.7	5.8	−0.35	Falling	Middle	2.2
2	30/06/2018	10:54	0.48	5.6	−0.8	Falling	Low	1.8
3	30/06/2018	10:54	0.6	5.6	−0.75	Falling	Low	1.8
4	02/08/2018	10:41	1.5	11.6	−1.3	Falling	Low	3.0
5	23/06/2018	10:54	0.8	9.3	0.5	Rising	High	2.5
6	06/12/2019	11:30	1.75	12	0.19	High	High	1.3
7	26/01/2020	11:00	0.43	7	−0.39	Falling	High	0.18
8	26/01/2020	11:00	0.56	8.3	0.22	Falling	High	0.22
9	26/01/2020	11:00	0.56	8.3	0.22	Falling	High	0.22

Fig. 1. Study sites along the Atlantic European coast (1–6) and the Western Mediterranean (7–9). Numbers refer to the sites described in Table 1.

3. Methodology

3.1. Definition of reference shorelines

The VHR images were used as ground truth to identify the instantaneous shorelines (defined as the water/land boundary). In most sites, the shorelines were photo-interpreted, as in the case of sites 4–9, for which the shorelines were manually digitised using GIS software as the line perceived as the highest position reached by the waves (Fig. 2, sites 4–9). On the contrary, the identification of the shoreline at the tidal Dutch beaches (Fig. 2, sites 1–3) was more complex. The images (both VHR Pléiades-1B and S2) were acquired during the falling tide making the photointerpretation of the shorelines difficult due to the presence of intertidal morphologies. In order to deal with that, supervised classification techniques were used in GIS to determine the water/land limit. The classified zone was limited to the emerged beach together with a

buffer of 200 m of water. In order to help with the classification process, the NDWI index (Gao, 1996) was defined from the existing bands (Red, Green, Blue, NIR) of the Pléiades imagery. Subsequently, 3 classes were defined: water, wet sand, and dry sand. The values obtained in the estimation of the a priori statistical separability among classes by the Jeffries-Matusita method were always greater than 1.97 (being 2 the maximum possible value) and the minimum value of the kappa coefficient was 0.96 (being 1 the maximum possible value). The limits between the aforementioned classes were classified as the shoreline (water/wet sand limit) and the wetline (wet/dry sand limit). The latter one was exclusively employed for interpretative purposes in the discussion section.

The test sites showed notable differences at the time of the analysis, related to the morphological characteristics mentioned above. Thus, Dutch beaches (Fig. 2, sites 1, 2, and 3) show a wide intertidal zone (wet or submerged at the moment of the image acquisition) associated with a gentle slope. On the contrary, Tarnos and SJDL (Fig. 2, sites 4, 5) show a very clear water/land boundary (even though Tarnos is at low tide). Mira VHR image was acquired during the high tide (Fig. 2, f) during swell conditions that lead to a wide wet zone.

3.2. Definition of SDSs

The satellite-derived shorelines were defined from the freely available optical Sentinel-2 imagery using the software SAET. This tool provided the framework for downloading the source S2 images as well as the algorithm to obtain the SDSs. The workflow followed four main phases (Fig. 3): image downloading, segmentation, approximate-pixel shoreline (hereafter APS) masking, and sub-pixel shoreline extraction following the algorithmic solution proposed by Pardo-Pascual et al. (2012). The workflow of the tool is described in detail by Palomar-Vázquez et al. (2023).

For the SDSs assessment, the SDS extraction was carried out by combining different S2 processing levels and extraction methods (Fig. 4). Just like the reference shorelines, the SDSs were defined as the instantaneous water/land interface. The workflow in SAET followed 4 steps.

Table 3

VHR images associated with the quasi-simultaneous S2 image employed in the SDS analysis. The characteristics of both the VHR and the S2 images are presented.

| Site	VHR satellite	Date VHR (dd/mm/yy)	Time VHR (UTC)	Date S2 (dd/mm/yy)	Time S2 (UTC)	Time diff. (h:m)
1	Pléiades-1B	30/06/2018	11:08	June 30, 2018	10:54	0:13
2	Pléiades-1B	30/06/2018	11:08	30/06/2018	10:54	0:14
3	Pléiades-1B	30/06/2018	11:09	30/06/2018	10:54	0:14
4	SPOT-6	23/06/2018	11:15	23/06/2018	11:05	0:09
5	Pléiades-1B	02/08/2018	10:41	02/08/2018	11:00	0:19
6	WorldView-2	06/12/2019	11:16	06/12/2019	11:30	0:14
7	SPOT-7	26/01/2020	10:23	26/01/2020	11:00	0:36
8	Pléiades-1A	26/01/2020	10:53	26/01/2020	11:00	0:06
9	Pléiades-1A	26/01/2020	10:50	26/01/2020	11:00	0:09
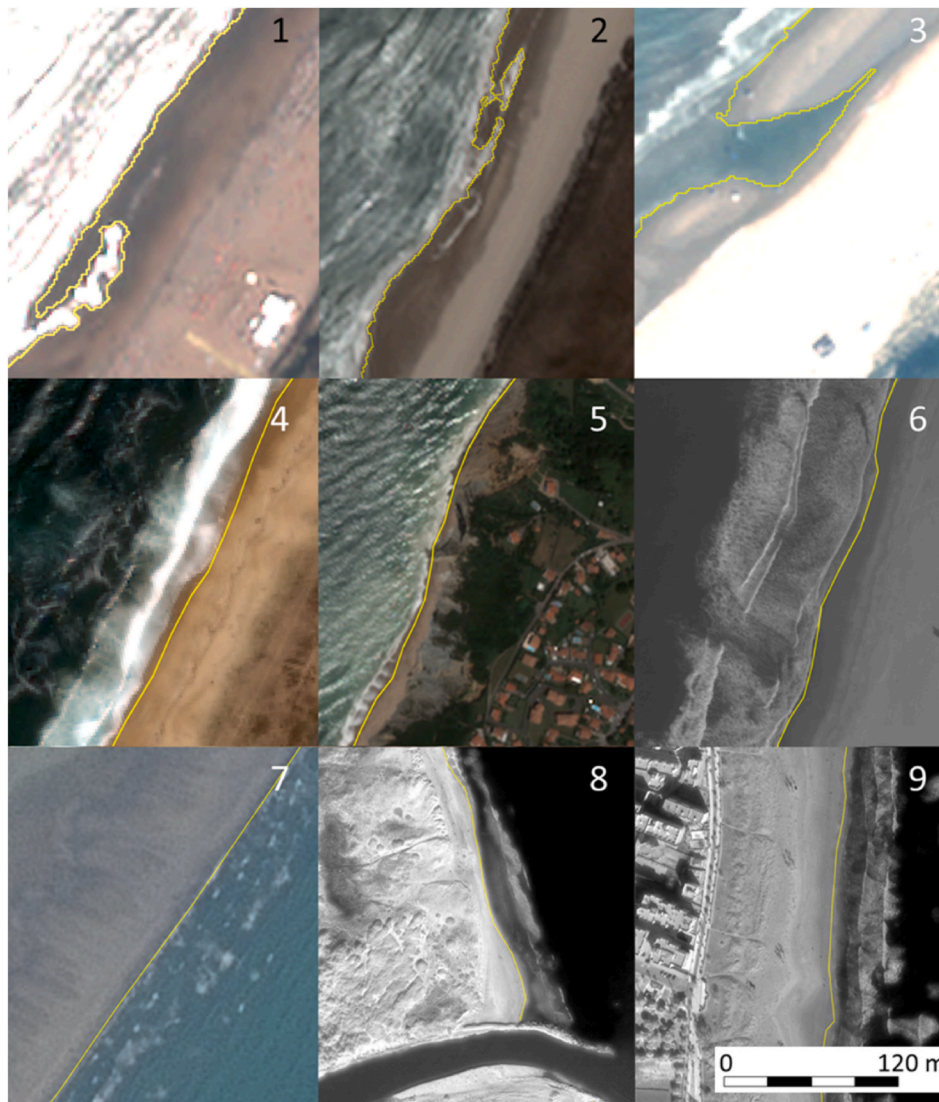
Fig. 2. Examples of the reference shorelines defined by image classification in (1) Texel, (2) Leiden, (3) The Hague; and in (4) Tarnos, (5) SJDL, (6) Mira, (7) Ebro, (8) Castellón, and (9) Valencia by photointerpretation. Pléiades-1A and 1 B © CNES (2018), distributed by Airbus DS, provided under COPERNICUS by the European Union and ESA, all rights reserved; SPOT 6 and 7 © Airbus DS (2018), provided under Copernicus by European Union and ESA, all rights reserved; WorldView-2 © Digital Globe, Inc. (2019), provided under COPERNICUS by the European Commission, ESA and European Space Imaging.

1 Image downloading. The S2 images, both with TOA and BOA processing levels, coincident with the VHR images were downloaded from the official provider via the Copernicus Open Access Hub (COAH).

2 Segmentation. In order to define the to define the water/land interface four APSs were obtained for each image from the MNDWI, AWEIsh, AWEInsh (Table 4) and SWIR 1 (short wave infrared band). The first three of them were binarized with a constant threshold of 0 whilst the thresholding of SWIR 1 band was accomplished by using the k-means method (Fig. 4). Furthermore, two morphological filters, erosion and dilation, were used over the previous water mask so as to define the water/land boundary.

3 APS masking. Considering the APS as input, SAET removed those pixels classified as clouds with the help of the cloud classification band of each image. Furthermore, the resulting layer was clipped according to the beach mask of European beach polygons provided by the Copernicus Land Monitoring Service (CLMS).

4 Sub-pixel shoreline extraction. Following the pixels defined by the APS, a kernel analysis was performed on the SWIR1 band following the method originally described in Pardo-Pascual et al. (2012). The reflectance of the pixels in the kernel of the APS was fitted with a 3D polynomial function so that the mathematical highest gradient edge (where the Laplacian equals 0) was considered to be the sub-pixel location of the shore. A kernel size of 5 × 5 and a polynomial degree of 3 have been set for the subpixel SDSs. This kernel increases the probability of finding the real inflexion line although the initial APS could have been placed too far because of the erosion/dilation morphological filters. Besides, a polynomial degree equal to 3 is less likely to give unstable polynomials (both when the polynomial is fit and when the Laplacian is calculated) which makes it more suitable for initial tests.

All four indices and bands used for segmentation were considered on both the images with the TOA and BOA processing levels. Once the images were binarized, two morphological filters, dilation or erosion, were used to define a continuous set of pixels that constituted the APS.

It must be noticed that sub-pixel extraction (the last step in Figs. 3 and 4) is not straightforward. In normal circumstances, the set of APS follows a clear line. Once the subpixel process is performed, a few anomalous points might appear, yet they are filtered at the last step. As
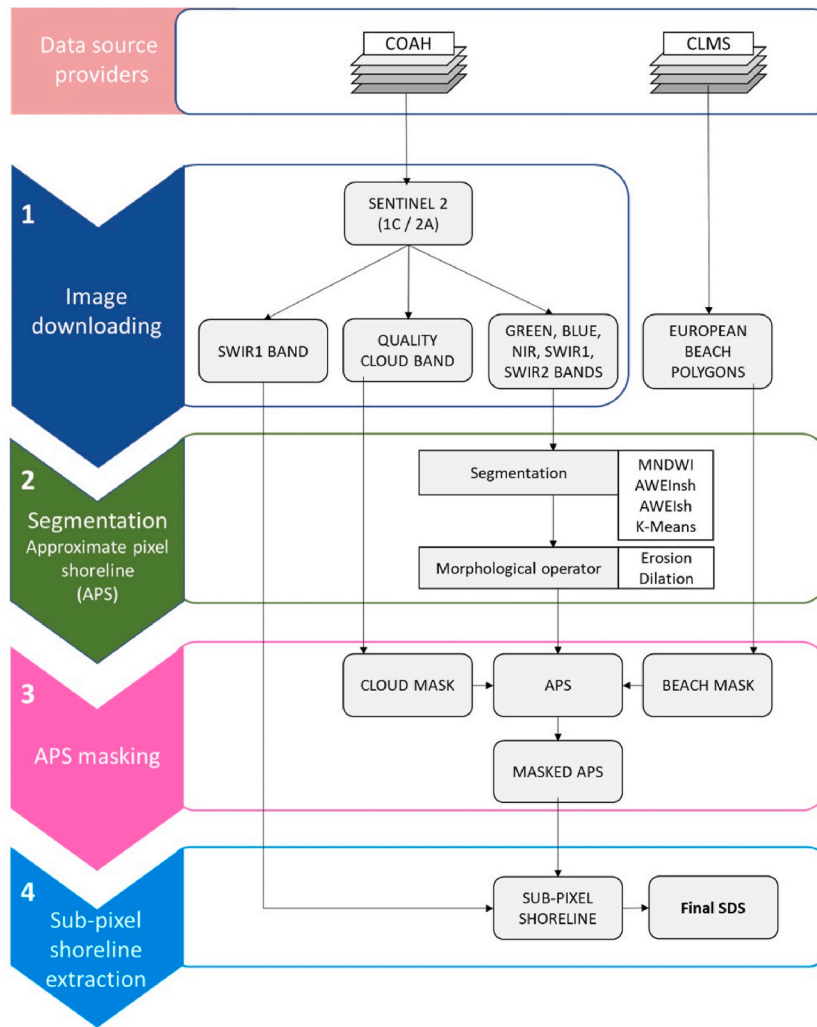
5

Fig. 3. SAET workflow to use Sentinel-2 imagery. The following acronyms are used in the workflow: COAH (Copernicus Open Access Hub); CLMS (Copernicus Land Monitoring Service); APS (Approximate-Pixel Shoreline).

explained in Sánchez-García et al. (2020), the minimum spanning tree (MST) method (Graham and Hell, 1985) is applied to remove outliers and obtain the final shoreline.

3.3. SDSs accuracy assessment

The position of each SDS extracted from S2 using SAET was compared with the reference position according to the ground-truth data, i.e., photo-interpreted/supervised-classified shorelines from VHR imagery. The accuracy (error) of each SDS was defined by measuring the shortest planimetric distance between the position of their vertices with respect to the reference line, and it was expressed as mean distance, bias and RMSE (root-mean-square error). For each test site and segmentation method the most efficient combination of image processing level and morphological filter was selected. Finally, the impact of the other variables was analysed. This makes it possible to evaluate (a) how important the segmentation method used for the identification of the water/land interface is, and (b) the influence of the beach morphology and the oceanographic conditions of each test site on the resulting errors.

4. Results

For each site, and considering both the TOA and BOA images, the shoreline position was extracted using 4 binarization options (band or index, and thresholding method). The original water binarized mask was eroded (seawards) or dilated (landwards) to detect the approximated pixel shoreline (APS). This led to 36 combinations in each site for a total of 144 evaluation cases (Fig. 5).

The magnitude of the errors appeared to be related to the specific conditions of each test site. Thus, the lowest biases appeared in the Mediterranean sites of Valencia and Castellón for certain specific solutions followed by slightly higher errors, but more stable, for all the solutions at the Bay of Biscay sites of Tarnos and SJDL. In Ebro, though the bias remained under 20 m, the deviation increased. Dutch beaches showed significant landward bias greater than 5 m, especially in Texel and The Hague. The errors in Mira were the highest both regarding bias and standard deviation for one specific solution (Fig. 5). Considering all the evaluations, in 4% of the cases the errors expressed as RMSE appeared below 5 m (Fig. 6). RMSE ranged between 5 and 10 m in 41% of the cases, 34% between 10 and 20, 17% between 20 and 50 m and 2.8% exceeded 50 m. However, major differences appeared depending on the type of binarization used. Nevertheless, when using AWEInsh, 97% of cases showed errors below 20 m, followed by k-means (83%), while MNDWI and AWEIsh (69.4%) performed worse.

Regarding the morphological filters, the employment of erosion or dilation was reflected in the magnitude of the errors within each test site (Fig. 7). On the contrary, the employment of BOA or TOA images showed a smaller influence on the accuracy of the SDSs. Thus, when
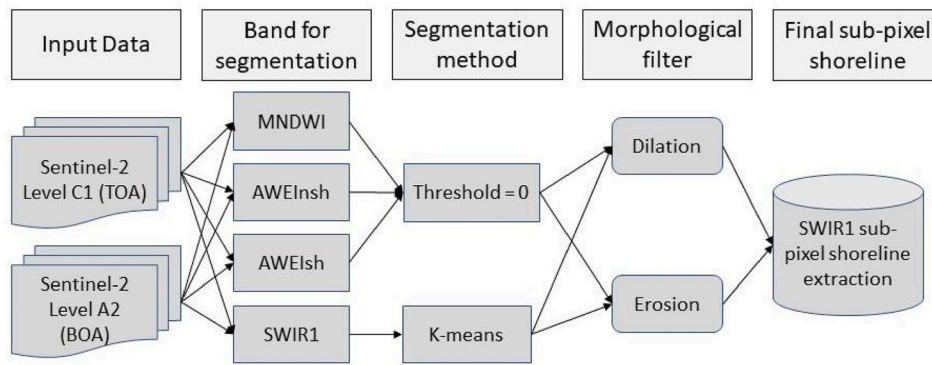
Fig. 4. Specific combinations of S2 processing levels and extraction methods to derive the SDSs at each test site.

Table 4

Indexes available for the initial binarization of the images, being NIR, SWIR1, SWIR2 and G the values of the pixel intensity in the near-wave, short-wave 1, short-wave 2 and green infrared bands respectively.

$$MNDWI = \frac{G - SWIR1}{G + SWIR1}$$

$$AWEIsh = B + (2.5 \bullet G) - 1.5 \bullet (NIR + SWIR1) - 0.25 \bullet SWIR2$$

$$AWEInsh = 4 \bullet (G - SWIR1) - (0.25 \bullet NIR + 2.75 \bullet SWIR1)$$

using AWEInsh to segment the land-sea space, the differences associated with the use of BOA or TOA images were generally low (the maximum difference in RMSE was 3.4 m). The differences were more significant when using dilation or erosion, reaching up to 9.88 m.

5. Discussion

The definition of SDSs with subpixel precision is of great interest among coastal monitoring techniques. Among the recent solutions proposed for the shoreline definition, SAET (Palomar-Vázquez et al., 2023) is a tool offering a wide variety of settings so as to obtain the shoreline with high accuracy and robustness. Understanding which SDSs are identified and defining the accuracy is a preliminary step for the application of the tool for coastal monitoring. Despite the recent progress in shoreline extraction techniques, the accuracy assessments employing in-situ data are often limited to low energy and/or microtidal coasts (e.g. Almeida et al., 2021; Hagenaars et al., 2018; Liu et al., 2017; Pardo-Pascual and Sanjaume, 2019; Sánchez-García et al., 2019, 2020) or, when considering higher energy and *meso*-macrotidal coasts, the assessments are mostly limited to a reduced number of locations or hydrodynamic conditions (e.g., Bishop-Taylor et al., 2019; Castelle et al., 2021; Vos et al., 2019a). The present paper constitutes the first evaluation of the SDS definition considering several different coastal types and using continuous reference data along the coast (Table 1) instead of local measurements or cross-shore profiles. The assessment considers very long coastal stretches, which allows the analysis of the accuracy in relation to specific characteristics of the coast.

The employment of AWEInsh = 0 constitutes the most robust binarization method for the different coastal typologies. Although AWEInsh did not show the lowest errors for every site (Fig. 5), it led to biases lower than 10 m (slightly overpassed in Castellón) showing that it is not significantly affected by the diverse characteristics of each site. This observation agrees with the evaluation performed by Bishop-Taylor, et al. (2019) and the satisfactory performance in the extraction of large shoreline datasets in intermittent shallow lakes using SHOREX (Palomar-Vázquez et al., 2022). Nonetheless, AWEInsh was expected to offer good results as it was designed to highlight the radiometric differences between the sea and the land (Feyisa et al., 2014) by giving more weight to the value of the SWIR band. This way, AWEInsh would

provide an improvement over the MNDWI index previously used with satisfactory results by other tools such as CoastSat (Vos et al., 2019a). AWEInsh with a constant value of 0 as proposed by Feyisa et al. (2014) makes it possible to perform the automatic thresholding required for defining the location of the APS. This enables the SDS extraction with a high degree of efficiency by making the human intervention required in SHOREX unnecessary for manually setting a threshold value (Cabezas-Rabadán et al., 2020) or for including a constant approximate shoreline (Sánchez-García et al., 2020). Regarding the other segmentation options, AWEIsh is an index specifically designed for areas with shadows, which are not present in the test sites. In turn, K-means is not an index but a segmentation method (MacQueen, 1967) aiming to provide a good local fit but struggling along larger territories as it is expected to happen with any generalisation of a thresholding solution (Bishop-Taylor et al., 2019).

Concerning the use of atmospherically corrected images (BOA or 2 A) they do not seem to offer a significant improvement in the results obtained (Fig. 7). Reducing the influence of the atmospheric effect on the reflectance values (ESA, 2015. E.S. Agency, 2015; Gascon et al., 2017) translates into a better detection of certain land coverages. Nevertheless, the differences are sometimes minor, mainly affecting the visible bands (Sola et al., 2018), and could interfere with the multispectral–in situ relationships due to losses of information during the correction (Medina-Lopez, 2020).

The accuracy of the SDS is not only affected by the shoreline detection methodology itself but also by the specific characteristics of each zone such as its morphology, land coverage and oceanographic conditions (Figs. 5–7). SDSs can be defined with a bias below 10 m in sites with a well-defined water/land boundary as in Tarnos, SJDL, Castellón and Valencia, generally showing standard deviations below 6 m (I.e., 25% of pixel size). Nevertheless, more complex coastal morphologies and oceanographic conditions can act as important inaccuracy drivers of the resulting SDSs. However, some solutions tested in this paper enable minimising the impact of these conditions. Thus, the application of the morphological filter of erosion shifts the SDS seaward while dilatation shifts it landward. This causes that in Texel, The Hague and Mira the errors are reduced when applying erosion. On the contrary in Valencia, Castellón, and to a lesser extent, in Ebro, SJDL, Tarnos and Leiden the opposite occurs, although, in these last four cases, the difference of magnitude of the errors when using dilatation or erosion is very small.

When comparing with other shoreline extraction methods currently available, the accuracies obtained in this assessment (Figs. 5–7) show similar magnitude levels despite SAET's methodological modifications to improve its robustness and efficiency. Thus, in the Mediterranean sites of Castellón and Valencia, the accuracy levels obtained by SAET are comparable to the 3.57 m and 3.01 RMSE for SDS derived from L8 and S2 imagery respectively when applying SHOREX on Cala Millor Beach, Balearic Islands (Sánchez-García et al., 2020). In more energetic and tidal coasts as those in the Bay of Biscay, the errors offer a slightly larger

Fig. 5. For each site, SDS errors are expressed as the mean distance and the standard deviation to the reference line when using the different indexes combined with the two morphological filters and levels of correction of the images. Errors larger than 20 m and 100 m are highlighted in orange and red respectively together with a shadowed background. It must be noticed that the vertical scale varies between graphs.

magnitude, similar to those obtained when using SHOREX (4.6 m and 5.8 m for S2 and L8) in the exposed and meso-tidal coast of South Portugal (Cabezas-Rabadán et al., 2020), and in the energetic and microtidal coast of central Chile (4.55 m RMSE for the combination of S2 and L8 according to Sánchez-García et al., 2019). In turn, these results are in line with those obtained by CoastSat (Vos et al., 2019b), with errors ranging from 7.2 m to 11.6 m RMSE at four microtidal beaches and 12.7 m RMSE on the meso-tidal and energetic coast of SW France. As for CASSIE, its accuracy was analysed at four nearby micro-tidal Brazilian beaches, showing an RMSE of 8.84 m though their evaluation only used a single L8 scene and the DGNSS reference information was acquired between 6 and 13 days after the satellite image. Hagenaars et al. (2018) analysed The Hague that was also analysed in the present paper. Three different scenes were analysed, each of them with different sea levels (SL) and wave heights (Hs). The correspondent errors were 1.3 ± 5.1 m for S2 (being SL = -0.48 m and Hs = 0.47 m), 8.5 ± 13.2 m for L8 (SL = -0.53 m, Hs = 1 m), 1 ± 13.9 m for L5 (SL = 0.12 m, Hs = 0.18 m). The application of SAET, with the AWEInsh = 0 solution, has led to -9.99 ± 5.6 m (-0.75 m SL and 0.6 m H). The bias of SAET has resulted to be worse, but with a better standard deviation. It must be noticed that the image analysed by SAET was taken at a lower sea level which exposed the intertidal area. The automatic extraction of the shoreline can occasionally result in very large errors caused by peculiar conditions. An example is the error recorded in Mira, where the combination of the MNDWI along with the dilation operator lead to a landward bias of -133 ± 93 m (Fig. 5). The analysis of the extraction workflow in this site (Fig. 8) shows that he MNDWI values identify a clear boundary that

could be marked as the shoreline (Fig. 8-B). Nevertheless, when applying a value 0 for the water index the resulting line defines the shoreline but also other inner boundaries. This type of error is probably caused by the existence of translucent cirrus clouds that affect the reflectance values in the coastal front, although it only affects the MNDWI index (and not other indexes) on the TOA images (and not BOA). From the aforementioned mask, both erosion and dilation morphological filters are performed (pink and green pixels in Fig. 8-D) to be used as input to derive the subpixel points that define the final shoreline. Subsequently, and as mentioned in the methodology section, the Minimum Spanning Tree (MST) algorithm is used to clean and select the proper points to draw the shoreline. The points found by MST for both the morphological filters of dilation and erosion lead to very different shorelines (8-F).

As mentioned, the initial thresholding could result in the APS not perfectly located. However, to avoid such coarse errors, SAET enables tuning a large combination of settings (I.e., kernel size, binarization method, and morphological filter) to adapt the shoreline extraction to the different coastal typologies. Furthermore, SAET also allows the inclusion of auxiliary data that can help to remove outlier points, as well as impeding the system to work outside the desired beach area. To do so, SAET uses land use/land cover layers available at pan-EU level that include sandy beach polygons (coastal Zone, 2018 from Copernicus Land Monitoring, https://land.copernicus.eu/local/coastal-zones/coastal-zones-2018) to ensure that no detected shoreline points are outside the areas of interest. The CLMS coastal zone database is still under validation, therefore some beaches are not properly mapped or a few
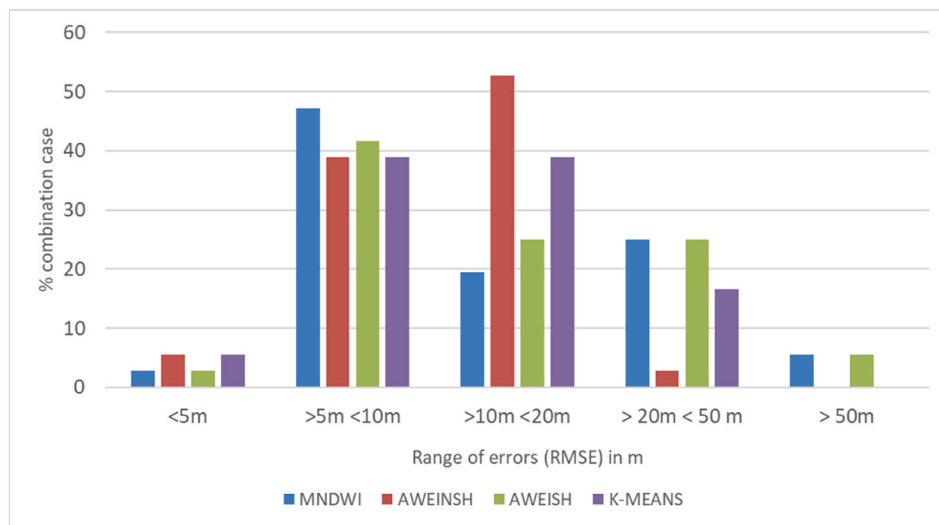

Fig. 6. For the different segmentation methods, the percentage of evaluation cases in which the error (expressed as RMSE) shows different ranges of magnitude.
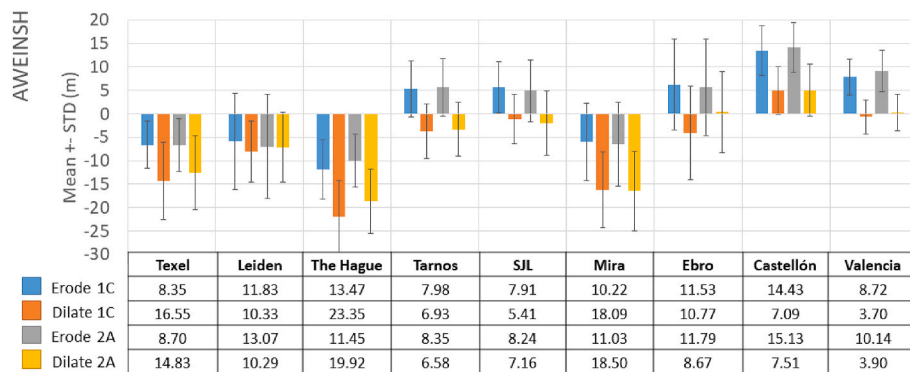

	Texel	Leiden	The Hague	Tarnos	SJL	Mira	Ebro	Castellón	Valencia
Erode 1C	8.35	11.83	13.47	7.98	7.91	10.22	11.53	14.43	8.72
Dilate 1C	16.55	10.33	23.35	6.93	5.41	18.09	10.77	7.09	3.70
Erode 2A	8.70	13.07	11.45	8.35	8.24	11.03	11.79	15.13	10.14
Dilate 2A	14.83	10.29	19.92	6.58	7.16	18.50	8.67	7.51	3.90

Fig. 7. Errors (in m) expressed in the figure as bias ± STD (box-and-whisker plots) and RMSE (as values in the table), at the different test sites when using (columns in different colours) TOA images and applying the AWEInsh index with a 0 threshold in combination with the erosion and dilation methods.
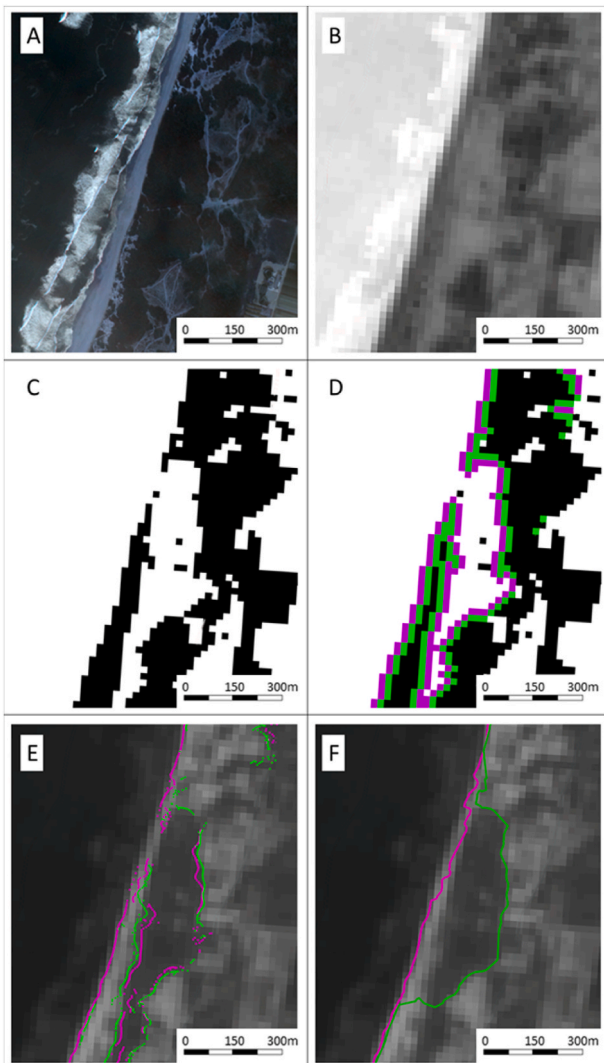
Fig. 8. Shoreline extraction in Mira. A) World-View 2 image (0.5 m pixel size) clearly shows the coastal conditions when the SDS has been extracted. B) MNDWI index and TOA processing. C) MNDWI binarized with value 0. D) Definition of the APS when using the morphological filters of erosion (pink) and dilation (green) over MDNWI mask. E) Subpixel candidate points derived over SWIR1 band. F) Final shoreline after applying MST. Background images: A) WorldView-2 © Digital Globe, Inc. (2019), provided under COPERNICUS by the European Commission, ESA and European Space Imaging, while B), E) and F) show the MNDWI mask obtained from Sentinel-2 products © CCME (2020), provided under COPERNICUS by the EU and ESA, all rights reserved.

beach polygons are misplaced In the case of the Mira site, a better definition of the boundaries of the beach resulted in the removal of the wrong points and to the variation of the error from -133 ± 93 m to 28.7 ± 14.6 m (Fig. 9).

The results are in line with Hagenaars et al. (2018) as the shoreline extraction is challenging in beaches with a very gentle slope (as the sites 1–3). In The Hague, the worst SDS accuracy appears when the shorelines are obtained using the AWEIsh index over the TOA images by dilating the water mask. These results are unexpected as AWEIsh is used in the presence of shadows that are not present in the analysed images. Additional validation is needed to understand if intertidal morphologies, saturated sand and puddles are treated by the algorithm as shadows.

Although the Hague has similar characteristics of Mira, the subpixel points are spread randomly instead of following two clear lines. AWEIsh index seems to be affected by the wet sand, leading to a landward displacement of the masked zone. As the APS in Fig. 10 has also been

obtained by dilating this mask, it seems difficult to locate the waterline, but the system detects boundaries between runnels (flooded channels) and intertidal bars. Therefore, it does not detect a completely wrong boundary as the identified limit can be defined as a shoreline. These results can be explained by the fact that the beach shows a very gentle slope and, consequently, the intertidal zone is more than 100 m wide (Fig. 10) with complex intertidal morphologies and water-saturated sands. The identified shoreline suggests that, due to the gentle slopes, similar levels of saturation can impede the identification of a clear boundary in the reflection values of the satellite images. Therefore, slight changes in the threshold used to binarize the image imply great displacements and a meaningless SDS. This effect was previously observed in the shoreline extraction on inner water bodies with gentle slopes and high soil moisture around the water body (Palomar-Vázquez et al., 2022). Through the given hypothesis, it seems clear that, in gently sloping beaches, minor changes in thresholding values may greatly affect the resulting SDSs. It could explain the different results associated with the use of atmospherically corrected images on the Dutch coast, which conversely shows no significant effects in the other sites. The hypothesis could also explain the constant landward bias of the SDSs as very saturated sands would have a similar spectral response to water (both on the indices and the SWIR1 band) making the detection of the instantaneous water line difficult. On the contrary, on steeper beaches, the saturated sand is unlikely to cover large stretches, and the position defined by the SDSs can be defined as a representation of a clear water/line interface, probably influenced by swash processes (Bishop-- Taylor et al., 2021; Cabezas-Rabadán et al., 2020, 2021). In any case, and independently of the type of beach, the water level and the run-up associated with the time of acquisition of the satellite image seem to play a key role in the location and meaning of the line extracted from the satellite (Castelle et al., 2021; Vitousek et al., 2023a). Despite the difficulty in making VHR images available, further assessments such as those presented in this paper may be useful in order to achieve a deeper comprehension of the reality represented by the SDSs, especially in tidal and energetic coasts. Beyond SDSs accuracy, their utility for characterising the morphological dynamics of a beach is still a matter of discussion. SAET obtains (with the limitations previously described) the instantaneous water/land position, therefore being affected by the instantaneous water level when the image is acquired. All the visual definitions of that interface contrast with datum-based shorelines. Their definition is substantially more complex as they require three-dimensional information on the beaches. Nevertheless, when reliable beachface slope and tidal data are available together with correct estimations of the setup and swash effects the SDSs can lead to good approximations of that datum-based shoreline (Vitousek et al., 2023b), therefore discarding the effects of water level changes.

Finally, it must be mentioned that the present assessment has been influenced by the accuracy of the reference shorelines. This can be especially noticeable on beaches of low gradient and wide tidal range (e. g., sites 1–3) in which their definition required the employment of classification methodologies. Although this procedure avoids subjective points of view, it seems clear that even these methods still need to be revised. In several beach segments the reference line, defined as the waterline (Fig. 10), presents such a complex morphology that it cannot be considered entirely appropriate to be compared with the SDSs. Likewise, manual photointerpretation can lead to errors associated with the subjectivity of the operator.

6. Conclusion

This work presents the first validation of SDSs obtained by using the new tool SAET for an automatic shoreline extraction. This research constitutes the first evaluation using as validation data the alongshore reference shorelines defined along large beach segments at different coastal typologies, including micro-tidal beaches along the Western Mediterranean and meso-tidal beaches along the Atlantic European
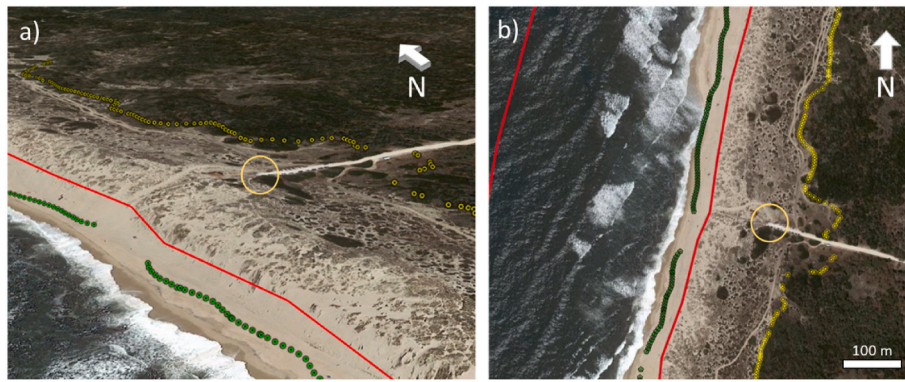
Fig. 9. Mira test site. a) 3D view of the shoreline and the dune foot. b) Aerial view. Red line shows the modified beach polygon. Yellow points identify the wrong "shoreline" location. Green points are the points correctly detected. Orange circle is only for reference purposes. Background image: Google Earth image from 5/26/2022 (Google LLC, 2023).
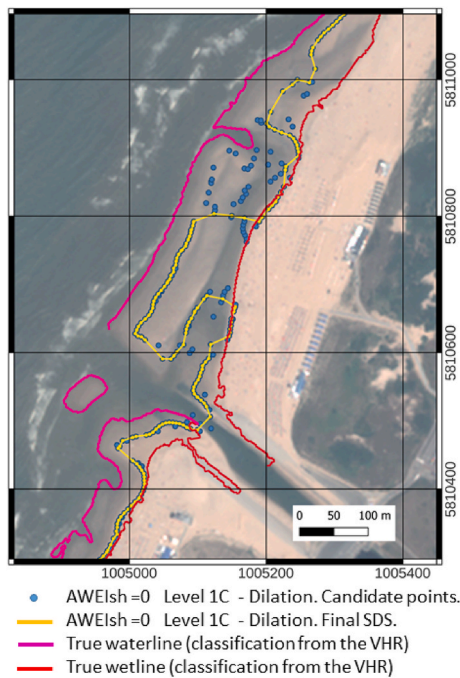

- ● AWEIsh =0   Level 1C - Dilation. Candidate points.
- — AWEIsh =0   Level 1C - Dilation. Final SDS.
- — True waterline (classification from the VHR)
- — True wetline (classification from the VHR)

Fig. 10. Detail of a challenging segment at the north part of The Hague, showing a) waterline (pink) and wetline (red) derived from the classification of the VHR Pleiades image. The candidate subpixel points (in blue) lead to the definition of the final shoreline (in yellow) after applying the MST procedure to remove outliers. Background image: Pléiades 1 B © CNES (2018), distributed by Airbus DS, provided under COPERNICUS by the EU and ESA, all rights reserved. Coordinate system: WGS84/UTM 30 N.

coast. Although this assessment is limited to a single date per site it constitutes a valuable complement to the evaluations based on video-derived (local) data due to the diversity of beach characteristics, tides and wave conditions analysed. The employment of VHR images for defining the reference shorelines has also made it possible to understand the variability of SDSs. The assessment confirms the utility of the SDS as a useful proxy for characterising the beach morphology, although they highlight the limitations to represent complex land/sea boundaries.

The SDSs show an average error that ranges between 3.7 m and 13.5 m (RMSE) among the different coastal types, therefore SAET is one of the most accurate and efficient shoreline extraction tools regardless of the shoreline typology. The tests carried out along coasts with variable morphological characteristics and oceanographic conditions show that SAET is a robust solution, with good accuracy levels even at meso-tidal and exposed coasts. Nevertheless, the algorithm still shows some limitations that may reduce the accuracy of the SDSs. When the land/water boundary is clear, SAET offers higher accuracies as it is based on subpixel edge refinement; but if saturated areas and complex intertidal morphologies appear, SAET is slightly biased landward from the reference line given that the transition is smooth, and the edge criteria might not be the most suitable. Tests also show how the segmentation methods employed for defining the approximate shoreline at the pixel level play a key role in the accuracy of the final SDSs defined at the subpixel level. The water index AWEInsh appears as the most accurate and robust solution for most of the test sites. The morphological filters play a smaller role in the accuracy, normally with systematic bias seaward or landward; when this difference becomes higher than 10 m, it is normally a symptom of complex scenarios. On the contrary, the atmospheric correction provided for the S2 images in general does not offer a substantial improvement in SDSs accuracy.

Considering the magnitude of the errors and its improved efficiency, SAET can be considered as a competitive tool for obtaining SDSs on diverse types of coasts from freely available optical satellite images, thus constituting a useful and efficient tool for the monitoring of coastal changes.

CRediT authorship contribution statement

J.E. Pardo-Pascual: Conceptualization, Methodology, Writing – review & editing, Formal analysis, Visualization, Funding acquisition. **J. Almonacid-Caballer:** Conceptualization, Methodology, Writing – original draft, Writing – review & editing, Formal analysis, Visualization. **C. Cabezas-Rabadán:** Conceptualization, Methodology, Writing – original draft, Writing – review & editing, Formal analysis, Visualization, Funding acquisition. **A. Fernández-Sarría:** Conceptualization, Methodology, Writing – review & editing, Formal analysis. **C. Armaroli:** Writing – review & editing, Funding acquisition, Project administration. **P. Ciavola:** Writing – review & editing. **J. Montes:** Writing – review & editing. **P.E. Souto-Ceccon:** Writing – review & editing. **J. Palomar-Vázquez:** Software, Conceptualization, Methodology, Writing – review & editing, Formal analysis, Visualization.

Declaration of competing interest

The authors declare that they have no known competing financial interests or personal relationships that could have appeared to influence the work reported in this paper.

Data availability

The authors do not have permission to share data.

Acknowledgements

References

Almonacid-Caballer, J., Pardo-Pascual, J.E., Ruiz, L.A., 2017. Evaluating Fourier cross-correlation subpixel registration in Landsat images. Rem. Sens. 9 (10), 1051. https://doi.org/10.3390/rs9101051.

Aranda-García, M., Gracia, F.J., Rodríguez-Santalla, I., 2022. Historical morphological changes (1956-2017) and future trends at the mouth of the Ebro River delta (NE Spain). Cuadernos de Investigación Geográfica 48 (2), 293–307. https://doi.org/10.18172/cig.5220.

Bergsma, E.W.J., Almar, R., 2020. Coastal coverage of ESA' Sentinel 2 mission. Adv. Space Res. 65 (11), 2636–2644. ISSN 0273-1177. https://www.sciencedirect.com/science/article/pii/S027311772030140X.

Bishop-Taylor, R., Sagar, S., Lymburner, l., Alam, i., Sixsmith, J., 2019. Sub-pixel waterline extraction: characterising accuracy and sensitivity to indices and spectra. Rem. Sens. 11 (24), 2984. https://doi.org/10.3390/rs11242984.

Bishop-Taylor, R., Nanson, R., Sagar, S., Lymburner, L., 2021. Mapping Australia's dynamic coastline at mean sea level using three decades of Landsat imagery. Rem. Sens. Environ. 267, 112734 https://doi.org/10.1016/j.rse.2021.112734.

Cabezas-Rabadán, C., Pardo-Pascual, J.E., Palomar-Vázquez, J., 2021. Characterizing the relationship between the sediment grain size and the shoreline variability defined from sentinel-2 derived shorelines. Rem. Sens. 13 (14), 2829. https://doi.org/10.3390/rs13142829.

Cabezas-Rabadán, C., Pardo-Pascual, J.E., Almonacid-Caballer, J., Rodilla, M., 2019c. Detecting problematic beach widths for the recreational function along the Gulf of Valencia (Spain) from Landsat 8 subpixel shorelines. Appl. Geogr. 110, 102047 https://doi.org/10.1016/j.apgeog.2019.102047.

Cabezas-Rabadán, C., Pardo-Pascual, J.E., Almonacid-Caballer, J., Palomar-Vázquez, J., Fernández-Sarría, A., 2019b. Monitorizando la respuesta de playas mediterráneas a temporales y actuaciones antrópicas mediante imágenes Landsat. GeoFocus: Rev. Int. Ciencia y Tecnol. Inf. Geográfica (23), 119–139.

Cabezas-Rabadán, C., Pardo-Pascual, J.E., Palomar-Vázquez, J., Fernández-Sarría, A., 2019a. Characterizing beach changes using high-frequency Sentinel-2 derived shorelines on the Valencian coast (Spanish Mediterranean). Sci. Total Environ. 691, 216–231. https://doi.org/10.1016/j.scitotenv.2019.07.084.

Cabezas-Rabadán, C., Pardo-Pascual, J.E., Palomar-Vazquez, J., Ferreira, O., Costas, S., 2020. Satellite derived shorelines at an exposed meso-tidal beach. J. Coast Res. 95 (SI), 1027–1031. https://doi.org/10.2112/SI95-200.1.

Casella, E., Drechsel, J., Winter, C., Benninghoff, M., Rovere, A., 2020. Accuracy of sand beach topography surveying by drones and photogrammetry. Geo Mar. Lett. 40, 255–268. https://link.springer.com/article/10.1007/s00367-020-00638-8.

Castelle, B., Masselink, G., Scott, T., Stokes, C., Konstantinou, A., Marieu, V., Bujan, S., 2021. Satellite-derived shoreline detection at a high-energy meso-macrotidal beach. Geomorphology 383, 107707. https://doi.org/10.1016/j.geomorph.2021.107707.

Duo, E., Fabbri, S., Grottoli, E., Ciavola, P., 2021. Uncertainty of drone-derived dems and significance of detected morphodynamics in artificially scraped dunes. Rem. Sens. 13 (9), 1823. https://www.mdpi.com/2072-4292/13/9/1823.

Elias, E.P., van der Spek, A.J., 2017. Dynamic preservation of Texel Inlet, The Netherlands: understanding the interaction of an ebb-tidal delta with its adjacent coast. Neth. J. Geosci. 96 (4), 293–317. https://doi.org/10.1017/njg.2017.34.

ESA, 2015. E.S. Agency, 2015. In: Sentinel-2 User Handbook.

Feyisa, G.L., Meilby, H., Fensholt, R., Proud, S.R., 2014. Automated Water Extraction Index: a new technique for surface water mapping using Landsat imagery. Rem. Sens. Environ. 140, 23–35. https://doi.org/10.1016/j.rse.2013.08.029.

Fontán-Bouzas, Á., Andriolo, U., Silva, P.A., Baptista, P., 2022. Wave impact analysis on a beach-dune system to support coastal management and nourishment works: the showcase of Mira, Portugal. Front. Mar. Sci. 9, 1–15. https://doi.org/10.3389/fmars.2022.861569.

Galiforni-Silva, F., Wijnberg, K.M., Mulder, J.P., 2022. Beach-dune development prior to a shoal attachment: a case study on Texel Island (NL). Mar. Geol. 453, 106907 https://doi.org/10.1016/j.margeo.2022.106907.

Galiforni-Silva, F., Wijnberg, K.M., de Groot, A.V., Hulscher, S.J., 2018. The influence of groundwater depth on coastal dune development at sand flats close to inlets. Ocean Dynam. 68, 885–897. https://doi.org/10.1007/s10236-018-1162-8.

Gao, B.C., 1996. NDWI—a normalized difference water index for remote sensing of vegetation liquid water from space. Rem. Sens. Environ. 58 (3), 257–266.

Gascon, F., Bouzinac, C., Thépaut, O., Jung, M., Francesconi, B., Louis, J., Lonjou, V., Lafrance, B., Massera, S., Gaudel-Vacaresse, A., Languille, F., Alhammoud, B., Viallefont, F., Pflug, B., Bieniarz, J., Clerc, S., Pessiot, L., Trémas, T., Cadau, E., De Bonis, R., Isola, C., Martimort, P., Fernandez, V., 2017. Copernicus Sentinel-2A calibration and products validation status. Rem. Sens. 9 (6), 584.

Graham, R.L., Hell, P., 1985. On the history of the minimum spanning tree problem. Ann. Hist. Comput. 7 (1), 43–57. https://doi.org/10.1109/MAHC.1985.10011. Jan.-March 1985.

Grases, A., Gracia, V., García-León, M., Lin-Ye, J., Sierra, J.P., 2020. Coastal flooding and erosion under a changing climate: implications at a low-lying coast (Ebro delta). Water 12, 346.

Guillen, J., Palanques, A., 1997. A shoreface zonation in the Ebro Delta based on grain size distribution. J. Coast Res. 867–878.

Guisado-Pintado, E., Jackson, D.W., Rogers, D., 2019. 3D mapping efficacy of a drone and terrestrial laser scanner over a temperate beach-dune zone. Geomorphology 328, 157–172.

Hagenaars, G., de Vries, S., Luijendijk, A.P., de Boer, W.P., Reniers, A.J., 2018. On the accuracy of automated shoreline detection derived from satellite imagery: a case study of the sand motor mega-scale nourishment. Coast. Eng. 133, 113–125.

Haralick, R.M., Sternberg, S.R., Zhuang, X., 1987. Image analysis using mathematical morphology. IEEE Trans. Pattern Anal. Mach. Intell. (4), 532–550.

Jiménez, J.A., Sánchez-Arcilla, A., Valdemoro, H.I., Gracia, V., Nieto, F., 1997. Processes reshaping the Ebro delta. Mar. Geol. 144, 59–79.

Jiménez, J.A., Sánchez-Arcilla, A., Bou, J., Ortiz, M.A., 1997b. Analysing short-term shoreline changes along the Ebro Delta (Spain) using aerial photographs. J. Coast Res. 1256–1266.

Liu, D., Yu, J., 2009. Otsu Method and K-Means, Ninth International Conference on Hybrid Intelligent Systems, pp. 344–349. https://doi.org/10.1109/HIS.2009.74, 2009.

Liu, Q., Trinder, J.C., Turner, I.L., 2017. Automatic super-resolution shoreline change monitoring using Landsat archival data: a case study at Narrabeen–Collaroy Beach, Australia. J. Appl. Remote Sens. 11 (1), 016036.

Luijendijk, A.P., Ranasinghe, R., de Schipper, M.A., Huisman, B.A., Swinkels, C.M., Walstra, D.J., Stive, M.J., 2017. The initial morphological response of the Sand Engine: a process-based modelling study. Coast. Eng. 119, 1–14.

MacQueen, 1967. Some methods for classification and analysis of multivariate observations. Proc. 5th Berkeley Symp. Math. Stat. Probability 1, 281–296, 1967.

Medina-Lopez, E., 2020. Machine learning and the end of atmospheric corrections: a comparison between high-resolution sea surface salinity in coastal areas from Top and Bottom of atmosphere sentinel-2 imagery. Rem. Sens. 12 (18), 2924. https://doi.org/10.3390/rs12182924.

Morichon, D., de Santiago, I., Delpey, M., Somdecoste, T., Callens, A., Liquet, B., liria, P., Arnould, P., 2018. Assessment of flooding hazards at an engineered beach during extreme events: biarritz, SW France,". J. Coast Res. 85 (sp1), 801–805. https://doi.org/10.2112/SI85-161.1.

Morton, R.A., Leach, M.P., Paine, J.G., Cardoza, M.A., 1993. Monitoring beach changes using GPS surveying techniques. J. Coast Res. 702–720.

Otsu, N., 1979. A threshold selection method from gray-level histogram. IEEE Transac. Syst. Man Cybernetics SMC-9 (No. 1), 62–66.

Palomar-Vázquez, J., Cabezas-Rabadán, C., Castañeda, C., Gracia, F.J., Fernández-Sarría, A., Priego-de-los-Santos, E., Pons, R., Pardo-Pascual, J.E., 2022. Inferring volumetric changes at a shallow lake from subpixel satellite-derived shorelines. Appl. Geogr. 149, 102792 https://doi.org/10.1016/j.apgeog.2022.102792.

Palomar-Vázquez, J., Pardo-Pascual, J.E., Almonacid-Caballer, J., Cabezas-Rabadán, C., 2023. Shoreline analysis and extraction tool (SAET): a new tool for the automatic extraction of satellite-derived shorelines with subpixel accuracy. Rem. Sens. 15 (12), 3198.

Pardo-Pascual, J.E., Almonacid-Caballer, J., Ruiz, L.A., Palomar-Vázquez, J., Rodrigo-Alemany, R., 2014. Evaluation of storm impact on sandy beaches of the Gulf of Valencia using Landsat imagery series. Geomorphology 214, 388–401.

Pardo-Pascual, J.E., García-Asenjo, L., Palomar-Vázquez, J., Garrigues-Talens, P., 2005. New methods and tools to analyze beach-dune system evolution using a real-time kinematic global positioning system and geographic information systems. J. Coast Res. 34–39.

Pardo-Pascual, J.E., Almonacid-Caballer, J., Ruiz, L.A., Palomar-Vázquez, J., 2012. Automatic extraction of shorelines from Landsat TM and ETM+ multi-temporal images with subpixel precision. Rem. Sens. Environ. 123, 1–11.

Pardo-Pascual, J.E., Sanjaume, E., 2019. Beaches in Valencian coast. In: Morales, J. (Ed.), The Spanish Coastal Systems. Springer, Cham. https://doi.org/10.1007/978-3-319-93169-2_10.

Pekel, J.F., Cottam, A., Gorelick, N., Belward, A.S., 2016. High-resolution mapping of global surface water and its long-term changes. Nature 540 (7633), 418–422.

Sánchez-Arcilla, A., Mösso, C., Sierra, J.P., Mestres, M., Harzallah, A., Senouci, M., El Raey, M., 2010. Climatic drivers of potential hazards in Mediterranean coasts. Reg. Environ. Change 11, 617–636, 2011.

Sánchez-García, E., Palomar-Vázquez, J.M., Pardo-Pascual, J.E., Almonacid-Caballer, J., Cabezas-Rabadán, C., Gómez-Pujol, L., 2020. An efficient protocol for accurate and massive shoreline definition from mid-resolution satellite imagery. Coast. Eng., 103732 https://doi.org/10.1016/j.coastaleng.2020.103732.

Sánchez-García, E., Briceño, I., Palomar-Vázquez, J., Pardo-Pascual, J., Cabezas-Rabadán, C., Balaguer-Beser, Á., 2019. Beach monitoring project on central Chile. In: 5ª Conferència sobre Morfodinâmica Estuarina e Costeira, pp. 49–50. MEC2019.

Sierra, J.P., González del Río, J., Flos, J., Sánchez-Arcilla, A., Movellán, E., Rodilla, M., Mösso, C., Martínez, R., Falco, S., Romero, I., 2001. Medición de parámetros físicos,

biológicos y químicos en el tramo estuarino del río Ebro, 2001 Ingenieria 8, 459–468 [Google Scholar].

Silva, R., Baptista, P., Veloso-Gomes, F., Coelho, C., Taveira-Pinto, F., 2009. Sediment grain size variation on a coastal stretch facing the North atlantic (NW Portugal). J. Coast Res. I, 762–766.

Sola, I., García-Martín, A., Sandonís-Pozo, L., Álvarez-Mozos, J., Pérez-Cabello, F., González-Audícana, M., Llovería, R.M., 2018. Assessment of atmospheric correction methods for Sentinel-2 images in Mediterranean landscapes. Int. J. Appl. Earth Obs. Geoinf. 73, 63–76.

Song, Y., Liu, F., Ling, F., Yue, L., 2019. Automatic semi-global artificial shoreline subpixel localization algorithm for Landsat imagery. Rem. Sens. 11 (15), 1779.

Stockdon, H.F., Holman, R.A., Howd, P.A., Sallenger Jr., A.H., 2006. Empirical parameterization of setup, swash, and runup. Coast. Eng. 53 (7), 573–588. https://www.sciencedirect.com/science/article/pii/S0378383906000044?via%3Dihub.

Strypsteen, G., Van Rijn, L.C., Hoogland, M.D., Rauwoens, P., Fordeyn, J., Hijma, M.P., Lodder, Q.J., 2021. Reducing aeolian sand transport and beach erosion by using armour layer of coarse materials. Coast. Eng. 166, 103871.

Talavera, L., Del Río, L., Benavente, J., Barbero, L., López-Ramírez, J.A., 2018. UAS as tools for rapid detection of storm-induced morphodynamic changes at Camposoto beach, SW Spain. Int. J. Rem. Sens. 39 (15–16), 5550–5567. https://www.tandfonline.com/doi/abs/10.1080/01431161.2018.1471549.

Viaña-Borja, S.P., Ortega-Sánchez, M., 2019. Automatic methodology to detect the coastline from Landsat images with a new water index assessed on three different Spanish mediterranean deltas. Rem. Sens. 11 (18), 2186.

Vitousek, S., Buscombe, D., Vos, K., Barnard, P.L., Ritchie, A.C., Warrick, J.A., 2023a. The future of coastal monitoring through satellite remote sensing. Cambridge Prisms: Coastal Futures 1, e10.

Vitousek, S., Vos, K., Splinter, K., Erikson, L., Barnard, P., 2023b. A model integrating satellite-derived shoreline observations for predicting fine-scale shoreline response to waves and sea-level rise across large coastal regions. J. Geophys. Res.: Earth Surf. https://doi.org/10.1029/2022JF006936.

Vos, K., Harley, M.D., Splinter, K.D., Simmons, J.A., Turner, I.L., 2019b. Sub-annual to multi-decadal shoreline variability from publicly available satellite imagery. Coast. Eng. 150, 160–174.

Vos, K., Splinter, K.D., Harley, M.D., Simmons, J.A., Turner, I.L., 2019a. CoastSat: a Google Earth Engine-enabled Python toolkit to extract shorelines from publicly available satellite imagery. Environ. Model. Software 122, 104528.

Vos, K., Splinter, K.D., Palomar-Vázquez, J., Pardo-Pascual, J.E., Almonacid-Caballer, J., Cabezas-Rabadán, C., Vitousek, S., 2023. Benchmarking satellite-derived shoreline mapping algorithms. Commun. Earth Environ. 4 (1), 345.

Wijsman, J.W.M., Verduin, E., 2011. To monitoring Zandmotor Delflandse kust: benthos ondiepe kustzone en natte strand (No. C039/11). IMARES.

Xu, H., 2006. Modification of normalised difference water index (NDWI) to enhance open water features in remotely sensed imagery. Int. J. Rem. Sens. 27 (14), 3025–3033.